thick to dissociate a large fraction of the incoming beam, they found that the fraction of the emerging beam in the uppermost levels had dropped only slightly. The small decrease does not necessarily imply a failure in the model, since the form of Eq. (8) and the philosophy in which it was used would also imply very large cross sections for excitation to neighboring vibrational levels —suggesting a mechanism for repopulation of the higher levels by an upward cascade. This characteristic of the cross section, however, remains to be demonstrated.

ACKNOWLEDGMENTS

We are grateful to Dr. C. M. Van Atta for supporting and encouraging this research. One of us (SNK) thanks Professor Burton J. Moyer and Professor A. C. Helmholz for the support and interest that enabled him to participate. We also thank Dr. John G. Conway, Dr. John R. Hiskes, and Dr. James M. Peek for several helpful discussions. Vincent J. Honey helped with the experimental work.

PHYSICAL REVIEW VOLUME 146, NUMBER 1 3 JUNE 1966

Coincidence Measurements of Large-Angle Ar^+-on-Ar Collisions*

QUENTIN C. KESSEL AND EDGAR EVERHART
Physics Department, The University of Connecticut, Storrs, Connecticut
(Received 23 November 1965)

Large-angle single collisions of keV-energy Ar^+ ions with Ar atoms are studied wherein both particles scattered from the same encounter are detected in coincidence. The scattered incident particle appears m-times ionized at angle θ and the recoiling target particle appears n-times ionized at angle ϕ. Values of m and n range from zero to eight. It is found that m and n are independent and uncorrelated, i.e., the distribution among charge states m is the same regardless of the charge state n seen in coincidence. An exception to this rule is seen in one region where the inelastic energy has multiple values. Relative probabilities for the (m,n) reaction are given for many data sets, with incident energies T_0 from 3 to 400 keV and for angles θ between 8° and 40°. The inelastic energy $\bar{Q}_{mn}$ associated with the (m,n) reaction is also measured for a number of values of m and n in each data set. It is found that a particular reaction does not have a fixed characteristic energy. Thus, for example, $\bar{Q}_{55}$ increases from 877 to 1473 eV depending on the violence of the collision. Average values of inelastic energy loss $\bar{Q}$ are plotted versus incident energy at various scattering angles, versus the average number of electrons lost in the collision, and versus the distance of closest approach. Values of $\bar{Q}$ range from 26 eV at $T_0=3$ keV, $\theta=8°$, to 2430 eV at $T_0=300$ keV, $\theta=40°$. The effects of thermal motion of the target atom, of finite instrumental resolution, and of a possible distribution in values of inelastic energy all combine to give "linewidth" effects. These are measured and discussed.

1. INTRODUCTION

COINCIDENCE-scattering measurements in atomic physics are a recent development. The first such experiment was reported by Afrosimov, Gordeev, Panov, and Fedorenko,[1] who studied Ar^+-Ar collisions at 12 and 50 keV by this technique and interpreted the phenomena observed. Preliminary results from a parallel experiment in our laboratory have been described[2,3] and these together with the present experiment offer evidence in support of a rather different interpretation.[4]

The reaction under study is

$$Ar^+ + Ar \rightarrow Ar^{+m} + Ar^{+n} + (m+n-1)e. \quad (1)$$

The incident ion is scattered to angle θ with charge $+m$ and the recoil target particle is found at angle ϕ with charge $+n$. The present experiment includes the energy range 3 to 400 keV at angles θ between 8° and 40° and measures m and n for particles originating from the same collision. The fractional probability $\bar{p}_{mn}$ of the (m,n) event is determined. Furthermore, the inelastic energy lost $\bar{Q}_{mn}$ is measured for reactions in which both m and n are specified.

The Ar^+-Ar collision has been the subject of many papers prior to these coincidence studies. Thus Fedorenko,[5] Kaminker and Fedorenko,[6] Carbone *et al.*,[7]

* This study was supported by the U. S. Air Force Office of Scientific Research.

[1] V. V. Afrosimov, Yu. S. Gordeev, M. N. Panov, and N. V. Fedorenko. Zh. Tekhn. Fiz. **34**, 1613 (1964); **34**, 1624 (1964); **34**, 1637 (1964) [English transl.: Soviet Phys.—Tech. Phys. **9**, 1248 (1965); **9**, 1256 (1965); **9**, 1265 (1965)]. Additional recent measurements by these same authors may be found in Zh. Tekhn. Fiz. **36**, 123 (1966) [English transl.: Soviet Phys.—Tech. Phys. **36** (to be published) (1966)], and in JETP Pis'ma v Redaktsiyu **2**, 153 (1965) [English transl.: JETP Letters **2**, 185 (1965)].

[2] E. Everhart and Q. C. Kessel, Phys. Rev. Letters **14**, 247 (1965).

[3] Q. C. Kessel, A. Russek, and E. Everhart, Phys. Rev. Letters **14**, 484 (1965).

[4] E. Everhart and Q. C. Kessel, following paper, Phys. Rev. **146**, 27 (1966).

[5] N. V. Fedorenko, Zh. Tekhn. Fiz. **24**, 784 (1954).

[6] D. M. Kaminker and N. V. Fedorenko, Zh. Tekn. Fiz. **25**, 2239 (1955).

[7] R. J. Carbone, E. N. Fuls, and E. Everhart, Phys. Rev. **102**, 1524 (1956).

Fuls *et al.*,[8] Jones *et al.*,[9] and Pivovar *et al.*,[10] have measured the differential-scattering cross section and the distribution among the charge states scattered at various angles. A series of papers by Russek *et al.*[11] have described a statistical model of the ionization process which has been successful in describing the ionization probabilities seen in the above results. The differential cross section data have been used by Lane and Everhart[12] to determine the interatomic potential energy function for Ar^+-Ar at close separations. The inelastic energy losses in the Ar^+-Ar collision were studied by Afrosimov and Fedorenko,[13] and by Morgan and Everhart.[14] However, coincidence measurements give much more detailed information, and several of the early experimental papers are rendered obsolescent.

The present paper describes the experiment and presents the data in a way which is independent of any conceptual model of the collision mechanism. A second paper,[4] immediately following, introduces and describes a model or framework which may be helpful in understanding these data.

2. THEORY OF THE MEASUREMENT

In Fig. 1 the incident particle, of initial energy T_0, has energy T_1 after scattering to angle θ and the target particle has energy T_2 after recoiling to angle ϕ. It is convenient to introduce $\beta=\theta+\phi$, where β is the angle between trajectories after scattering. The effect of a finite Q is to decrease β from the value β_0 it would have if Q were zero.

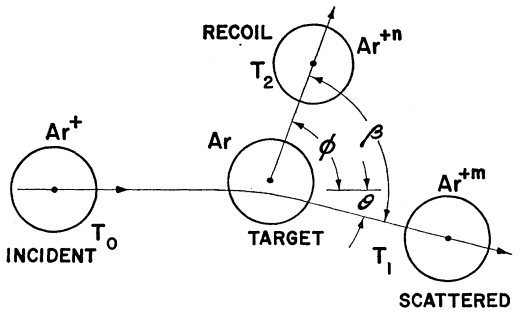

FIG. 1. The collision.

As shown in the Appendix,

$$T_1/T_0=\sin^2(\beta-\theta)/\sin^2\beta, \tag{2}$$

and

$$T_2/T_0=\gamma\sin^2\theta/\sin^2\beta, \tag{3}$$

where the incident to target mass ratio is γ. Since

$$Q/T_0=1-(T_1/T_0)-(T_2/T_0), \tag{4}$$

it is seen that simultaneous measurement of T_0, θ, and β suffices to measure Q. In the experiment one detector is fixed at the angle θ and the other detector is swept to find the angle β at which the corresponding recoil particles arrive. When $Q/T_0\ll1$ then Q is linearly proportional to the difference between β and β_0. Thus for $\gamma=1$, where $\beta_0=\pi/2$, the excellent approximation

$$Q/T_0=(\pi/2-\beta)\sin2\theta \tag{5}$$

may be used, as derived in the Appendix.

There is a range of values β which give coincidence counts for a fixed θ, giving rise to "linewidth" effects. This is due partly to natural linewidth, partly to the effects of thermal motion of the target particle, and partly due to instrumental resolution. These are discussed in Sec. 5C.

3. APPARATUS AND PROCEDURE

The present apparatus has the same function as that previously described by Afrosimov *et al.*,[1] but differs markedly in mechanical design because one apparatus is an "inside-out" version of the other. In the first apparatus[1] there was a small target gas chamber connected to two movable detecting chambers by means of flexible bellows. In the present apparatus, however, the target gas chamber is large and includes movable, evacuated enclosures for detectors. The present design has the advantage that there are no bellows to limit the angular motion of either detector.

A. Mechanical Construction

Figure 2 shows a schematic diagram of the apparatus. The magnetically analyzed ion beam from the accelerator enters through the collimating holes *a*, *b*, and *c* on the left. The ion beam passes from the evacuated region through hole *c*, which is of 0.07 cm diameter, into the gas target region. Although the target gas chamber is large, 74 cm diam, hole *c* is only 0.43 cm from the scattering center.

The two triangular boxes, although surrounded by target gas, are evacuated through massive hollow connecting rods. These connect to concentric evacuated pipes which permit rotation about the scattering center using large-diameter ball bearings and seals in a vacuum manifold.

The scattered incident particles at angle θ are collected through slits *d* and *e*, which are 0.023 and 0.044 cm wide, respectively.

[8] E. N. Fuls, P. R. Jones, F. P. Ziemba, and E. Everhart, Phys. Rev. **107**, 704 (1957).
[9] P. R. Jones, F. P. Ziemba, H. A. Moses, and E. Everhart, Phys. Rev. **113**, 182 (1959); P. R. Jones, P. Costigan, and G. Van Dyk, *ibid.* **129**, 211 (1963); P. R. Jones, N. W. Eddy, H. P. Gilman, A. K. Jhaveri, and G. Van Dyk, *ibid.* (to be published).
[10] L. I. Pivovar, M. T. Novikov, and V. M. Tubayev, Zh. Eksperim. i Teor. Fiz. **46**, 471 (1964) [English transl.: Soviet Phys.—JETP **19**, 318 (1964)].
[11] A. Russek and M. T. Thomas, Phys. Rev. **109**, 2015 (1958); **114**, 1538 (1959); J. B. Bulman and A. Russek, *ibid.* **122**, 506 (1961); A. Russek, *ibid.* **132**, 246 (1963).
[12] G. H. Lane and E. Everhart, Phys Rev. **120**, 2064 (1960).
[13] V. V. Afrosimov and N. V. Fedorenko, Zh. Tekhn. Fiz. **27**, 2557 (1957) [English transl.: Soviet Phys.—Tech. Phys. **2**, 2391 (1957).
[14] G. H. Morgan and E. Everhart, Phys. Rev. **128**, 667 (1962).

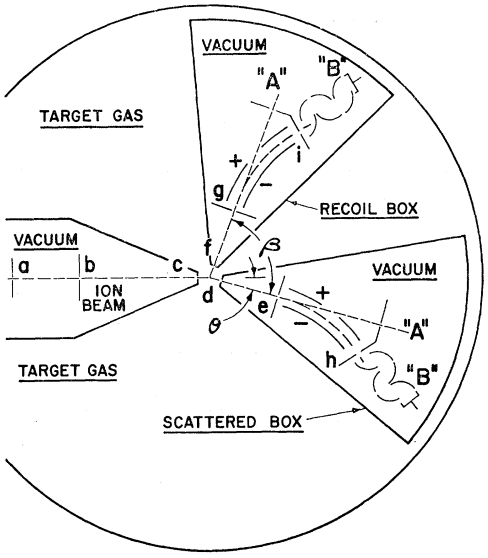

FIG. 2. Coincidence-scattering apparatus.

The slit d is only 0.43 cm from the scattering center, and this distance is the same for slit f of the recoil box. Collimating slit f and hole g in the recoil box are 0.059 and 0.117 cm wide, respectively.

Although the back wall of the large chamber is deformed 0.018 cm by atmospheric pressure, all the accurately aligned parts are mounted from the same flange and maintain their relative position. Mechanical alignment is such that the incident collimation and the recoil and target collimation are concentric and coplanar to within 0.0013 cm (0.0005 in.).

Final alignment of the zero-indices for both θ and β is accomplished by passing the collimated incident-ion beam through both the scattered box and the recoil box in turn. The center values of both these angles are measured to $\pm 0.03°$.

B. Charge-State Analysis

Upon passing through the collimator of their respective triangular detector boxes, the scattered and recoil ions (or atoms) enter an electrostatic analyzer. Ions are deflected by an electrostatic field and follow the curved path shown in Fig. 2. These ions pass through slit h (or i) into a secondary-electron multiplier in position B, which counts these particles. Neutral particles pass through a hole in the analyzer. When the detector is swung to position A the neutral particles are counted. This same position of the detector, but with no voltages on the analyzer plate, allows counting of all particles irrespective of their charge state, i.e., the "total" counting rate. With the detector returned to position B, and with the proper sequence of voltages applied to the analyzer plates, the counting rate for each ionization state can be measured in turn.

The detectors are Dumont type SPM-03-309 14-stage secondary electron multipliers. The first dynode is grounded so that there is no post-acceleration of the charge states. These detectors are operated under conditions for which there are at least 95 output pulses for each 100 incident particles regardless of the charge state.

C. Time of Flight

It is evident on considering Fig. 2 that the two particles from the same collision, having different velocities, do not arrive simultaneously at their respective detectors. The flight-path is 21.6 cm and the time difference, of the order of a few microseconds, must be allowed for. The output pulses of the detectors (after amplification and shaping) enter magnetostrictive delay lines. There is a fixed 15-μsec delay in the recoil channel, and a variable 12 to 35-μsec delay in the scattered-particle channel. The relative delay can thus be set from -3 to $+20$ μsec.

The delay time is set to the computed time of flight to within 0.1 μsec and the coincidence gate is about 0.5 μsec wide. Three electronic counters are used, one for the scattered-particle counts, one for the recoil-particle counts, and one for the coincidence counts. In practice the counting rate in either channel is of the order of 10 to 5000 counts/sec and the coincidence counting rate is of the order of 1 to 100 counts/sec. At the higher counting rates one makes a correction for random coincidences.[15]

In earlier studies the counts of neutral scattered atoms were inseparable from those due to photons, which were also counted by the detectors. These photons, presumably isotropic, arise from collisions in the target region and only a negligible fraction of these correspond to collisions at the particular scattering angles θ and β. Of course their time of flight is different also. The coincidence channel contains no photon counts, thus removing this source of error.

D. Single-Collision Conditions

It is essential that the observed collision products be the result of single collisions. A second collision becomes likely when the path through the target gas is too long or when the target gas pressure is too high. Avoiding a second collision requires a careful adjustment of experimental conditions since the total cross section for (say) charge exchange is far larger than the differential cross section for the rare large-angle collisions under study here. The practical way to ensure single collision conditions is to measure $\bar{P}_i$, the percentage of the particles in ionization state i in either the scattered or recoil beam, as a function of target gas pressure. At high pressures $\bar{P}_i$ depends on pressure, but single collision conditions are attained at a sufficiently low pressure where $\bar{P}_i$ becomes constant. Such a plot appears in Fig. 3(a) where it is seen that 5×10^{-4} Torr is the

[15] See, for example, R. D. Evans *The Atomic Nucleus* (McGraw-Hill Book Company, Inc., New York, 1955), p. 791–793.

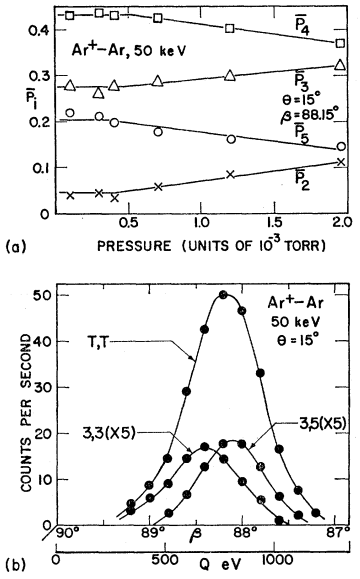

FIG. 3. (a) Charge-state probabilities $\bar{P}_i$ are plotted versus target gas pressure for recoil particles from Ar^+-Ar collisions, $T_0=50$ keV, $\theta=15°$, $\beta=88.15°$. (b) Profiles of coincidence counts versus recoil angle β.

highest tolerable pressure. In this case the total path length in gas is only 0.86 cm. The advantage of a short path is evident. If the total path in gas were five times as large, say 4.3 cm, then the maximum tolerable pressure would be 10^{-4} Torr and the counting rates would be $\frac{1}{5}$ as large. In practice each data set would then require 10 days instead of 2 days as at present.

We find that our early work at large angles[8] was evidently taken at somewhat too high a pressure and improved $\bar{P}_1$ values are to be given here. In fact, the data for Fig. 1 of our recent letter[2] were also taken at too high a pressure, although the discussion in that letter is not changed by more accurate data.

E. Target-Gas Purity

One advantage of coincidence measurements is that small impurities in the target gas cause no errors and no coincidence counts. Because the mass of the target particle is different from the mass of the impurity atom the coincidence counts are not found at the same pairs of angle (θ,ϕ) and there are no counts from this source. It might be remarked that diatomic target particles do not lend themselves to coincidence measurements when the collision is so violent as to dissociate the target molecule. The two target particles plus the scattered incident particle do not leave coplanar or at predictable angles in a 3-body break-up.

F. Procedure

The set of data taken at 50 keV, $\theta=15°$ is described as an example. The computed delay (1.85 μsec in this case) is set into the delay lines and checked by watching the coincident count rate as this delay is adjusted. The detectors in both boxes in Fig. 2 are set to position A and with no voltages on the analyzer the "total-total" coincidence counts C_{TT} are determined. This is a data set wherein C_{TT} is measured at a function of β as shown in Fig. 3(b). The number of noncoincidence counts in the scattered channel is used as a monitor. It is seen from Eq. (5) that Q and $90°-\beta$ are linearly related, so that Fig. 3(b) is also a plot of C_{TT} versus Q as indicated by the second scale on the abscissa. The peak of this curve determines a weighted average Q value, namely $\bar{Q}$, which is identical with $\bar{Q}_{TT}$. The values of T_1 and T_2 corresponding to θ and to the center, $\bar{\beta}_{TT}$, of the peak are then computed using Eqs. (2) and (3). These values are necessary to determine the schedule of voltages for the charge-state analyzers in the two boxes. Appendix B shows that one does not change the schedule of analyzer voltages as β is varied while T_0 and θ are held constant.

A pressure run, as illustrated in Fig. 3(a) is then taken, and if necessary, the C_{TT} data of Fig. 3(b) would be repeated if the initial choice of pressure had proved to be too high. The inelastic energy loss $\bar{Q}_{mn}$ of the individual (m,n) reactions can now be measured. Thus, for example, the scattered box may be set to pick up $m=3$ and the recoil box may be set for $n=5$ so that the (3,5) coincidence counts C_{35} are measured, versus β, as in Fig. 3(b). This gives a center value $\bar{\beta}_{35}$ from which the corresponding $\bar{Q}_{35}$ is readily calculated. Measurements of $\bar{\beta}_{mn}$, which determines $\bar{Q}_{mn}$ are carried out for a number of (m,n) values. In this 50 keV, $\theta=15°$ example the (3,3), (3,4), (3,5), (4,4), (4,5), and (5,5) combinations are studied. Interchanging m and n makes no difference, i.e. (3,5) data and (5,3) data are the same. When $\bar{\beta}_{mn}$ (or $\bar{Q}_{mn}$) is plotted versus U_{mn}, which is the ionization energy deficit in Eq. (1), the data lie on fairly straight lines. This line is interpolated or extrapolated to get an approximate value of $\bar{\beta}_{mn}$ for rare combinations such as (2,2), (2,6), (5,6), etc.

Having values for $\bar{\beta}_{mn}$ it is then possible to take data for a correlation matrix as in Table I. This gives the number N_{mn} of counts in each (m,n) category, each count being taken with the recoil box set at the value $\bar{\beta}_{mn}$, indicated in the table, where the count rate for the reaction in question is a maximum. The table also gives the experimental $\bar{Q}_{mn}$ values.

The matrix of Table I could have been taken by holding the incident beam constant and counting for a predetermined time. However, it is more accurate to use a procedure which removes the effect of incident beam fluctuations. First the recoil box is set in position A for "totals" and the number of *noncoincident* counts in the scattered box in various charge states m is recorded until a predetermined number (say 10 000) of noncoincident totals arrive in the recoil box. Such a measurement gives a schedule of the relative number of noncoincident counts for each charge state in the scattered box, and this schedule is independent of the ion beam fluctuations. Then, in taking the data for the matrix, one counts the coincidence (m,n) events until the scheduled number of counts for charge state m are reached in the noncoincident scattered box channel.

TABLE I. Correlation and Q-value matrix for 50 keV, 15° data. For each specified pair of charge states (m,n) the first entry is the number of such events recorded, and the second entry is the angle $\bar{\beta}_{mn}$ in degrees at which recoil-particle detector was set as explained in the text. The third entry gives measured values of $\bar{Q}_{mn}$ in eV.

$m=$	1	2	3	4	5	6
	0	2	12	22	24	2
$n=1$	88.65	88.60	88.50	88.40	88.35	88.05
	...	...	...	...	...	...
	4	10	103	207	141	29
$n=2$	88.60	88.55	88.45	88.35	88.20	88.00
	...	...	...	...	...	...
	12	79	576	1102	565	74
$n=3$	88.50	88.45	88.40	88.25	88.10	87.95
	...	...	685±22	745±21	...	...
	22	204	1114	1695	705	79
$n=4$	88.40	88.35	88.25	88.10	88.00	87.80
	...	...	...	805±16	...	...
	11	142	626	788	272	19
$n=5$	88.35	88.20	88.10	88.00	87.85	87.65
	...	...	814±18	861±17	916±22	...
	7	31	96	63	19	2
$n=6$	88.05	88.00	87.95	87.80	87.65	87.40
	...	...	...	...	...	...

This procedure gives accurate relative values of counts N_{mn} despite fluctuations of a factor of two in the incident beam current.

G. Data Reduction, Definitions

The random count rate correction[15] has already been made in the N_{mn} entries in Table I. The relative probability $\bar{p}_{mn}$ of the (m,n) event within each data set is found by normalizing:

$$\bar{p}_{mn}=N_{mn}/\sum_{m,n} N_{mn}. \quad (6)$$

The relative probability $\bar{P}_i'$ of charge state i being formed among the scattered particles is

$$\bar{P}_i'=\sum_n \bar{p}_{in} \quad (7)$$

and the corresponding probability $\bar{P}_i''$ of charge state i being found among the recoil particles is

$$\bar{P}_i''=\sum_m \bar{p}_{mi}. \quad (8)$$

Experimentally it is found that $\bar{P}_i'=\bar{P}_i''$ within data scatter. Thus,

$$\bar{P}_i=\tfrac{1}{2}[\bar{P}_i'+\bar{P}_i''] \quad (9)$$

gives the best value $\bar{P}_i$ for charge state i being found among either the scattered or recoil component.

The average charge $\bar{m}$ of the scattered component within each data set is

$$\bar{m}=\sum_i i\bar{P}_i' \quad (10)$$

with a similar equation for $\bar{n}$.

Bars are placed over many experimental quantities to indicate that the measured quantity may be an average. Thus $\bar{Q}_{mn}$ is an average inelastic energy, since there may conceivably be a distribution of inelastic energies associated with the (m,n) event. Placing the bar over the experimental quantities also keeps these separate from the related unaveraged quantities in the following paper.[4]

4. DATA

Many combinations of energy T_0 and scattering angle θ are studied, ranging from 3 to 400 keV and from 8° to 40°.

Table II gives the values of $\bar{Q}_{mn}$ for representative cases. The complete data are available from American Documentation Institute.[16] The table shows the average inelastic energy associated with the (m,n) event and is obtained using Eqs. (4) or (5) with data such as that shown in Fig. 3(b). The (T,T) or (total-total) notation refers to the average value of inelastic energy measured irrespective of charge state, and $\bar{Q}_{TT}$ is identical with $\bar{Q}$. The accelerator has a maximum of 250 kV, and some of the data[16] extending up to 400 keV are obtained using Ar^{2+} ion beams, as noted in the tables. Where there is overlap, as at 200 keV, the $\bar{Q}$ data for the Ar^{+} and Ar^{2+} beams agree fairly well.

At $T_0=25$ keV, $\theta=16°$ and in a few other data sets a triple-peak is seen in the Q data,[17] as shown in Fig. 4. In these cases each peak can be studied separately and the superscript a, b, or c in the tables refer to the successive peaks. This structure has been interpreted[3] and is further discussed in the following paper.[4]

Table III gives the probabilities $\bar{p}_{mn}$ for each (m,n)

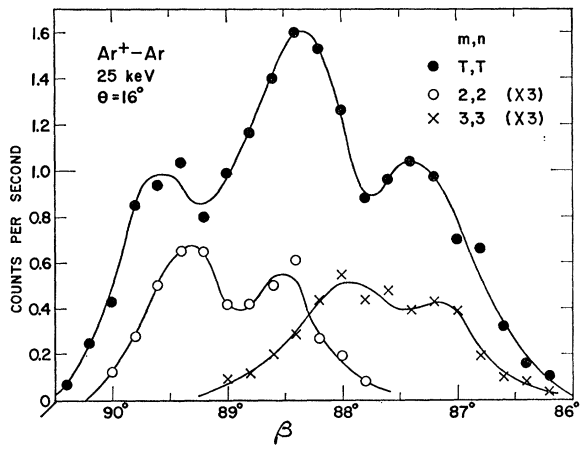

FIG. 4. Profiles of coincidence counts versus recoil angle β in the triple-peak region.

[16] The complete set of tables, including also supplementary text and figures from Ref. 4, has been deposited as Document No. 8798 with the ADI Auxiliary Publications Project, Photoduplication Service, Library of Congress, Washington, D. C. 20036. A copy may be secured by citing the Document number and by remitting $2.50 for photoprints or $1.75 for 35-mm microfilm. Advance payment is required. Make checks or money orders payable to Chief, Photoduplication Service, Library of Congress.

[17] This triple structure appears also at 12 keV, 38° and at 50 keV, 7°. It was first seen by Morgan and Everhart (Ref. 14) and then carefully investigated by Afrosimov *et al.* (Ref. 1). Reference 3 and parts of Ref. 4 are concerned with the interpretation of this phenomena.

TABLE II. Inelastic-energy-loss values $\bar{Q}_{mn}$ for Ar^+-Ar collision for reactions where charge states m and n after collision are both specified. The notation T,T (or total-total) refers to measurements of average Q wherein all particles are counted, irrespective of charge. Thus $\bar{Q}_{TT}\equiv\bar{Q}$. The incident ion energy T_0 and angle θ are given for each data set. These are representative data. The complete tables are available from American Documentation Institute (Ref. 16).

T_0,θ	m,n	$\bar{Q}_{mn}$ (eV)	m,n	$\bar{Q}_{mn}$ (eV)
6 keV, 8°	T,T	57±3	1,1	55±3
	0,1	36±3	2,1	79±4
	1,0	30±4		
25 keV, 8°	T,T	94±2	1,2	91±5
	0,1	27±5	1,3	127±5
	0,2	70±7	2,2	123±5
	1,0	29±5	2,3	167±7
	1,1	60±5		
25 keV, 16°	T,T[a]	90±17	2,2[b]	353±7
	T,T[b]	379±10	2,3[c]	362±9
	T,T[c]	613±14	2,3[c]	636±14
	1,1[a]	62±6	3,3[b]	468±6
	2,2[a]	160±7	3,3[c]	647±10
25 keV, 40°	T,T	696±9	3,4	704±16
	3,2	625±30	4,4	737±17
	3,3	646±18	4,5	805±18
50 keV, 15°	T,T	779±9	4,4	805±16
	3,3	685±25	4,5	861±17
	3,5	814±18	5,5	915±25
	4,3	745±20		
100 keV, 10°	T,T	905±12	4,4	845±25
	3,3	700±25	4,5	925±25
	4,3	790±25	5,5	995±25
150 keV, 20°	T,T	1620±30	6,6	1660±100
	5,5	1340±90	7,7	2000±100
200 keV, 10°	T,T	1430±30	5,6	1400±60
	T,T[d]	1340±40	5,7	1600±60
	4,4	1030±70	6,6	1560±60
	5,4	1100±50	7,7	1900±60
	5,5	1260±60		
200 keV, 20°	T,T	2030±70	6,6	1850±110
	T,T[d]	1920±70	7,7	2160±90
	5,5	1470±180	8,8	2340±180
300 keV, 20°	T,T[d]	2180±140		
300 keV, 40°	T,T[d]	2430±200		
400 keV, 10°	T,T[d]	2260±120		

[a] Data correspond to the low value, Q^{I}, in cases where more than one value is found.
[b] Data correspond to the intermediate value Q^{II}.
[c] Data correspond to the high value Q^{III}.
[d] Data taken using Ar^{2+} as incident ion.

combination in representative data sets and is raw material for a discussion of (m,n) correlations and ionization probabilities. Complete tables are available.[16] Thus each grouping within Table III is a normalized and condensed version of a data matrix such as given in the example of Table I. Also listed in Table III are the average charges $\bar{m}$ and $\bar{n}$, computed as in Eq. (10), and the total number of events $\Sigma_{m,n}N_{mn}$. Experimentally it is found that $\bar{m}=\bar{n}$ in every case, indicating that the one-electron deficiency is equally likely to be found on either particle after the collision.

Under each data set is a row of the $\bar{P}_i$ values shown in parentheses (where the values of i is the same as the value of m at the head of the column). These are computed using Eqs. (7)–(9) from the corresponding $\bar{p}_{mn}$ values.

TABLE III. The relative probability $\bar{p}_{mn}$ of the (m,n) event is given for data sets wherein the incident energy and scattering angle are specified. The number of individual collisions or events in the sample studied for each data set is noted as are the average values $\bar{m}$ and $\bar{n}$. At the foot of each data set the ionization probabilities $\bar{P}_i$ are shown in parenthesis. These are representative data. The complete tables are available from American Documentation Institute (Ref. 16).

6 keV, 8° ($\bar{m}=1.02$, $\bar{n}=1.15$, total events=309):

$m=$	0	1	2	3
$n=0$		0.1003	0.0453	0.0000
$n=1$	0.0841	0.4531	0.0809	0.0000
$n=2$	0.0388	0.1586	0.0227	0.0000
$n=3$	0.0065	0.0097	0.0000	0.0000
$\bar{P}_i$	(0.138)	(0.670)	(0.184)	(0.008)

25 keV, 16° ($\bar{m}=1.89$, $\bar{n}=1.73$, total events=379)[a]:

$m=$	0	1	2	3	4
$n=0$		0.0312	0.0165	0.0188	0.0029
$n=1$	0.0162	0.0939	0.1684	0.0377	0.0029
$n=2$	0.0091	0.0892	0.2541	0.0807	0.0085
$n=3$	0.0047	0.0289	0.0883	0.0268	0.0000
$n=4$	0.0000	0.0047	0.0082	0.0079	0.0000
$\bar{P}_i$	(0.050)	(0.284)	(0.489)	(0.161)	(0.018)

25 keV, 16° ($\bar{m}=2.51$, $\bar{n}=2.63$, total events=318)[b]:

$m=$	0	1	2	3	4	5
$n=0$		0.0076	0.0000	0.0038	0.0000	0.0000
$n=1$	0.0000	0.0055	0.0284	0.0537	0.0172	0.0000
$n=2$	0.0000	0.0315	0.1177	0.1533	0.0431	0.0057
$n=3$	0.0038	0.0553	0.1600	0.1148	0.0229	0.0057
$n=4$	0.0038	0.0138	0.0618	0.0464	0.0219	0.0000
$n=5$	0.0000	0.0076	0.0080	0.0093	0.0038	0.0000
$\bar{P}_i$	(0.010)	(0.113)	(0.364)	(0.372)	(0.129)	(0.020)

25 keV, 16° ($\bar{m}=3.12$, $\bar{n}=3.12$, total events=209)[c]:

$m=$	1	2	3	4	5
$n=1$	0.0000	0.0000	0.0192	0.0099	0.0000
$n=2$	0.0083	0.0052	0.0950	0.0447	0.0114
$n=3$	0.0000	0.1070	0.2513	0.1194	0.0036
$n=4$	0.0000	0.0488	0.1708	0.0748	0.0114
$n=5$	0.0000	0.0052	0.0140	0.0000	0.0000
$\bar{P}_i$	(0.019)	(0.166)	(0.516)	(0.278)	(0.023)

50 keV, 15° ($\bar{m}=3.84$, $\bar{n}=3.86$, total events=8859):

$m=$	1	2	3	4	5	6
$n=1$	0.0000	0.0002	0.0013	0.0025	0.0027	0.0002
$n=2$	0.0004	0.0011	0.0116	0.0234	0.0159	0.0033
$n=3$	0.0014	0.0089	0.0651	0.1246	0.0638	0.0084
$n=4$	0.0025	0.0230	0.1259	0.1916	0.0797	0.0089
$n=5$	0.0012	0.0161	0.0708	0.0891	0.0307	0.0022
$n=6$	0.0008	0.0035	0.0108	0.0071	0.0021	0.0002
$\bar{P}_i$	(0.007)	(0.057)	(0.285)	(0.427)	(0.200)	(0.025)

100 keV, 10° ($\bar{m}=4.32$, $\bar{n}=4.35$, total events=4026):

$m=$	2	3	4	5	6	7
$n=2$	0.0000	0.0025	0.0099	0.0084	0.0035	0.0005
$n=3$	0.0005	0.0139	0.0467	0.0591	0.0199	0.0010
$n=4$	0.0065	0.0532	0.1565	0.1441	0.0298	0.0020
$n=5$	0.0094	0.0596	0.1500	0.1172	0.0179	0.0020
$n=6$	0.0045	0.0179	0.0353	0.0174	0.0035	0.0005
$n=7$	0.0005	0.0020	0.0025	0.0020	0.0000	0.0000
$\bar{P}_i$	(0.023)	(0.145)	(0.396)	(0.352)	(0.077)	(0.007)

150 keV, 20° ($\bar{m}=5.79$, $\bar{n}=5.85$, total events=1474):

$m=$	3	4	5	6	7	8
$n=3$	0.0000	0.0027	0.0054	0.0068	0.0014	0.0000
$n=4$	0.0014	0.0081	0.0136	0.0312	0.0149	0.0027
$n=5$	0.0014	0.0271	0.0461	0.1058	0.0760	0.0109
$n=6$	0.0095	0.0299	0.1085	0.1547	0.0706	0.0149
$n=7$	0.0068	0.0217	0.0583	0.0733	0.0407	0.0081
$n=8$	0.0000	0.0027	0.0176	0.0217	0.0054	0.0000
$\bar{P}_i$	(0.018)	(0.082)	(0.259)	(0.391)	(0.209)	(0.042)

[a] Data correspond to the low value Q^{I} in cases where more than one value is found.
[b] Data correspond to the intermediate value Q^{II}.
[c] Data correspond to the highest value Q^{III}.

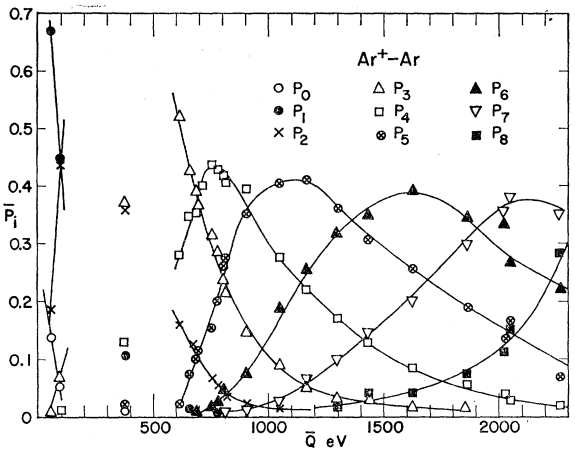

FIG. 5. Charge state probabilities $\bar{P}_i$ are plotted versus the average inelastic energy $\bar{Q}$ for large-angle Ar^+-Ar collisions. The data points between 100 and 600 eV are not connected by empirical lines because the phenomena is discontinuous in that region.

Experimentally it is found here that $\bar{P}_i$ is a function only of $\bar{Q}$ as shown in Fig. 5. The two gaps in this plot are related to the triple peak phenomena. Thus $\bar{P}_i$ for the lowest peak matches data with $\bar{Q}$ in the range of 0 to 100 eV, the middle peak contributes $\bar{P}_i$ for a single $\bar{Q}$ of 380 eV, and the $\bar{P}_i$ values for the highest peak fit in with all other data with $\bar{Q}$ above 600 eV.

The data on "linewidths" is presented in Sec. 5C.

5. DISCUSSION

Here the data are reduced and replotted in various ways which are independent of any interpretation of the collision process. In this way the empirical facts and relationships are kept separate from the discussion and speculations of the following paper,[4] which interpret these data in terms of a model. There are three distinct aspects of the data—the Q measurements, the (m,n) correlations, and the linewidths. These are discussed in turn.

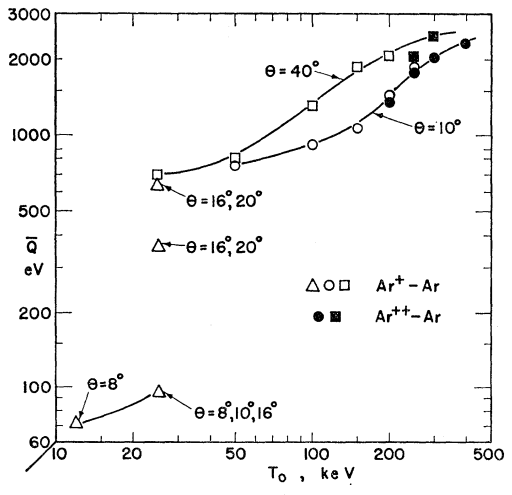

FIG. 6. For Ar^+-Ar collisions the average inelastic energy loss $\bar{Q}$ is plotted versus the incident energy T_0 with contours of constant scattering angle θ. Values of $\bar{Q}$ which are 26 eV for 3 keV, 8°, and 57 eV for 6 keV, 8° lie off the graph and are not shown.

A. Q Measurements

The average inelastic energy increases, generally, as either the energy T_0 or scattering angle θ increases. This is shown in Fig. 6 which plots $\bar{Q}$ versus T_0 with contours of constant θ. The triple-peak region contributes gaps on the left side of this plot. Additional activity, wherein $\bar{Q}$ rises rapidly with T_0, is seen in the 100 to 300-keV region of T_0. The high-energy data were taken with Ar^{++} ions incident and these data join smoothly with the Ar^+ data. Evidently in these violent collisions, where 5 to 8 electrons are lost by each atom, it makes little difference in $\bar{Q}$ whether or not there is one less electron on the incident ion. There is a suggestion of a plateau, or asymptotic limit, to $\bar{Q}$ of about 2500 eV for T_0 in excess of 400 keV.

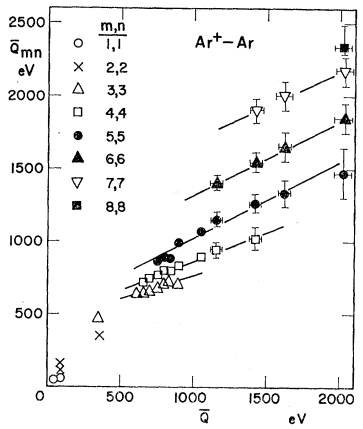

FIG. 7. For Ar^+-Ar collisions individual $\bar{Q}_{mn}$ values are plotted versus average inelastic energy loss $\bar{Q}$.

It is interesting to plot the individual $\bar{Q}_{mn}$ values for each data set versus the corresponding average $\bar{Q}$ as in Fig. 7. To avoid cluttering the figure, values are shown only for the cases where m and n are equal. A very significant fact is that the $\bar{Q}_{mn}$ values *are not independent of* $\bar{Q}$. Thus $\bar{Q}_{55}$, for example, increases from 877 to 1473 eV depending on the violence of the collision. Particular reactions do not have characteristic inelastic energies and this fact must be explained by a successful model.

Table II indicates that the $\bar{Q}_{mn}$ values in each data set depend on the total number of electrons lost and not, particularly, on the individual (m,n) values. Within each data set $\bar{Q}_{02}\approx\bar{Q}_{11}$, $\bar{Q}_{35}\approx\bar{Q}_{44}$, $\bar{Q}_{46}\approx\bar{Q}_{55}$, etc. Thus Fig. 8 is a meaningful condensation of data in showing $\bar{Q}_{mn}$ plotted versus $m+n-1$, the number of electrons lost in the particular (m,n) reaction. Here the triple-peak region (the points indicated as $\times$) contributes three discrete lines. Low-energy data yield other lines which drop at the lowest energies, and the high-energy data give a sequence of lines spaced even higher on this plot.

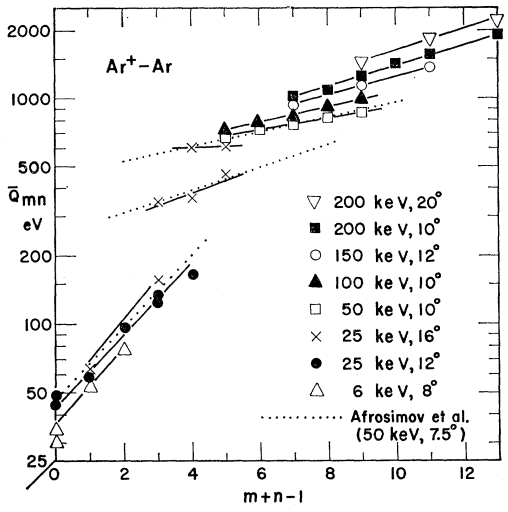

FIG. 8. Values of $\bar{Q}_{mn}$ are plotted versus $m+n-1$, which is the number of electrons lost in the (m,n) collision. Here the $\bar{Q}_{mn}$ are averages of several values where $m+n-1$ is constant.

The data of Afrosimov, Gordeev, Panov, and Fedorenko[1] are indicated by the dotted lines in Fig. 8. They were taken at 50 keV, $7\frac{1}{2}°$, in the middle of the triple-peak region, and the agreement is good. In their work[1] a number of $\bar{Q}_{mn}$ values were measured, but over-all average $\bar{Q}$ values were not given and individual $\bar{p}_{mn}$ values were not listed. For this reason it is not possible to show their data on the other figures. Their data and interpretation are further discussed in the following paper.[4]

Figure 9 is similar to the preceding figure except that average values are plotted. This plot of $\bar{Q}$ versus $\bar{m}+\bar{n}-1$ also shows data by Morgan and Everhart.[14] A discontinuity is seen between the high-energy and the low-energy data and it would require a downward displacement of several hundred eV to cause the upper branch to appear as an extension of the lower branch of the data curve. The dashed curve in Fig. 9 shows, for comparison, that portion of the inelastic energy loss which is due to spectroscopic energies. Knowing the spectroscopic energy deficit U_{mn} for each (m,n) reaction of Eq. (1) and the relative probabilities $\bar{p}_{mn}$ from Table II one can compute the weighted average spectroscopic energy deficit $\bar{U}$ using

$$\bar{U}=\sum_{m,n}\bar{p}_{mn}U_{mn} \qquad (11)$$

for each of the several data sets. The space between the dashed line and the $\bar{Q}$ data is thought to represent excess kinetic energy of the emitted electrons plus a contribution due to residual excitation with photon emission. This excess energy is of particular interest theoretically.[4]

In several Ar^+-Ar studies[1,7–10,14] it has been useful to determine how the data depend on R_0, the distance of closest approach. This distance is computed, approximately, from a classical trajectory for the collision using the appropriate screened-Coulomb-interaction potential energy. Details of the calculation have appeared in a paper by Everhart *et al.*[18] There has been experimental verification of the suggested potential.[7,11] For each of the data sets of Table II the corresponding value of R_0 is calculated. This appears as the abscissa on Fig. 10 where the ordinate is $\bar{Q}$. At any particular energy the largest R_0 value corresponds to the smallest scattering angle θ, and conversely. The triple-peak region shows as a break or step in the $\bar{Q}$ data at $R_0=0.23$ Å, at which distance the L shells of the two argons have interpenetrated to some extent. The other rapid rise, at about 0.09 Å, occurs before the two K shells have yet come into contact. A similar figure, but based on noncoincidence data appears as Fig. 7 of the Morgan and Everhart[14] paper. One significant facet of Fig. 10 is that all the data do not fall on a single line on this plot. Although the $\bar{Q}$ values depend strongly on R_0, there is also a dependence on the relative velocity of the colliding particles.

It should be noted that the several $\bar{Q}_{mn}$ values within any particular data set of Table II are interrelated. Thus $\bar{Q}_{35}$, for example is close to the average of $\bar{Q}_{33}$ and $\bar{Q}_{55}$, and in general

$$\bar{Q}_{mn}\approx\tfrac{1}{2}(\bar{Q}_{mm}+\bar{Q}_{nn})\,. \qquad (12)$$

It is expected that any model describing these collisions should be in approximate accordance with this experimental result.

Although the emphasis in this work has been on the more violent collisions where many electrons are lost, there are a few entries in Table II concerned with charge exchange or scattering without change of charge. For 3-, 6-, 12-, and 25-keV scattering at 8°, the (0,1) and (1,0) reactions have inelastic energies in the range 26 ± 8 to 45 ± 17 eV. These values indicate that a high

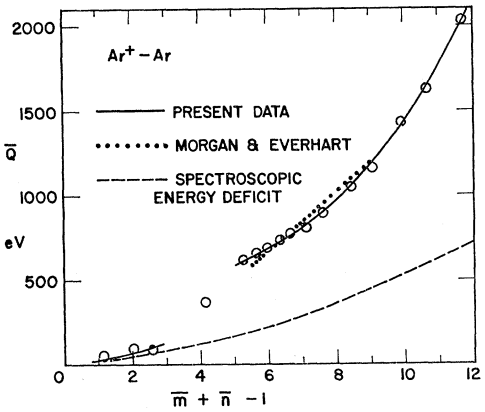

FIG. 9. For each data set the over-all average $\bar{Q}$ values in each data set are plotted versus the average number of electrons lost in that data set $\bar{m}+\bar{n}-1$.

[18] E. Everhart, G. Stone, and R. J. Carbone, Phys. Rev. **99**, 1287 (1955).

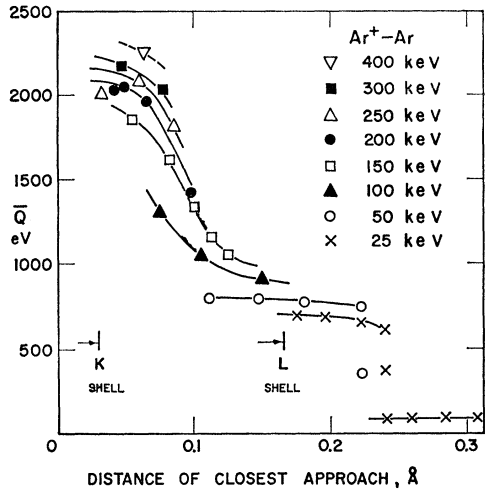

FIG. 10. Average inelastic energy loss $\bar{Q}$ is plotted versus R_0, the distance of closest approach (measured in angstroms), with incident energy T_0 as a parameter. The radii of the K and L shells of one argon atom are indicated to show scale.

level of excitation occurs without loss of electrons under these conditions.

B. Correlation between m and n

The $\bar{p}_{mn}$ values in Table III are here examined to determine to what extent, if any, the n value is related to the m value in the same collision.

If there were complete correlation then a given value of m would imply a particular value of n. This is clearly not in accordance with Table III, for then there would be only one entry in each row or column of each data set.

At the other extreme, if there were no correlation at all, then the distribution among the charge states n would be independent of m, and conversely. Figure 11(a) plots data from Table III showing $\bar{p}_{mn}$ values plotted versus n with contours of constant m for a typical data set. The striking result is that all contours have nearly the same relative proportions. This is shown again in Fig. 11(b) which plots the same data except the $\hat{p}_{mn}$ is a renormalized quantity such that $\Sigma_n \hat{p}_{mn}=1$ for each value of m. The fact that these distributions are all nearly the same shows that there is little, if any, correlation between m and n. This was first noted in a recent letter.[2]

When there is no correlation, a simple consequence is that $\bar{p}_{mn}$ may be predicted using

$$\bar{p}_{mn}=\bar{P}_m\bar{P}_n. \tag{13}$$

Here $\bar{P}_m$ and $\bar{P}_n$ are obtained by setting i equal to m, and then n in turn, in the values of $\bar{P}_i$ listed for each data set in Table III. Although the $\bar{P}_i$ values are derived from partial sums over the $\bar{p}_{mn}$ data, Eq. (13) is not an identity and holds only if there is no correlation. The solid points in Fig. 11(a) are computed using Eq. (13) and the agreement with the data is good.

The above result is unexpected. One might have thought that in events where m was higher than average one would find n to be lower than average, and vice versa, but such is not the case. In fact, Eq. (13) can be used with the $\bar{P}_i$ values to predict all the $\bar{p}_{mn}$ values in each data set of Table III with excellent over-all agreement. Any model for these collisions must be consistent with this empirical result.

There is a striking exception to this general agreement with Eq. (13). In the triple-peak region illustrated in Fig. 4 it is found that the $\bar{p}_{mn}$ data for the middle peak do not fit Eq. (13). These data correspond to the 25 keV, 16° case in Tables II and III where the superscript b denotes the middle-peak values. In this case there is a particular form of correlation wherein the $\bar{p}_{mn}$ values of the middle peak are predictable from the $\bar{p}_{mn}$ values of the first and third peaks. This has been discussed in a recent letter[3] and is further treated in detail in Sec. 6 of the following paper.[4] A slight amount of this same sort of correlation has been found in the data sets for 150 keV, 12° and 20°, indicating possible unresolved structure in that region.[19]

C. Linewidths

Widths of the experimental profiles such as the plot of C_{TT} versus β and also Q in Fig. 3(b) have been determined for all the data sets. Throughout this section the phrase "half-width" will refer to half the width of the profile measured at $1/e$ times the peak height. In Fig. 12(a) the half-width δQ of the C_{TT} profile is plotted versus T_0 for representative angles θ.

There are three effects contributing to δQ: First, there is instrumental half-width broadening δQ_a. This depends on the effective angular resolution half-width $\delta\beta_a$ which arises from the finite aperture sizes of the incident, scattered, and recoil collimators. It is found that, at large angles and high energies, instrumental broadening predominates and that all lines there asymptotically

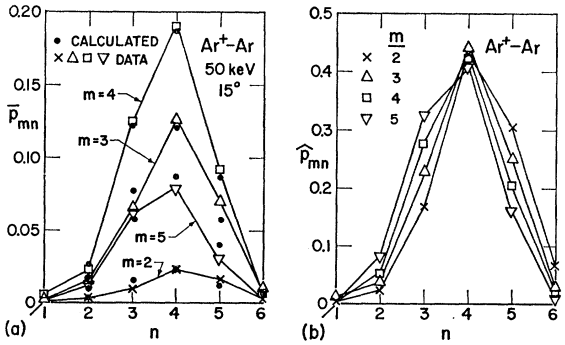

FIG. 11. (a) The probability $\bar{p}_{mn}$ of the (m,n) reaction is plotted versus n with contours of constant m. These data are for 50 keV, 15°. (b) Same, except that renormalized values $\hat{p}_{mn}$ are plotted as explained in the text.

[19] Q. C. Kessel, Ph.D. thesis, University of Connecticut, 1966 (unpublished).

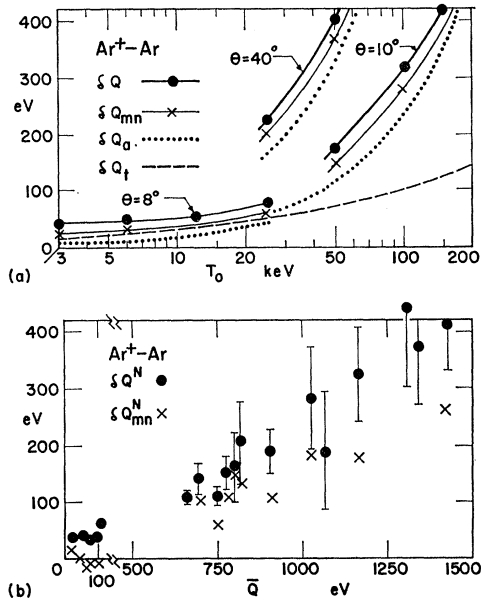

FIG. 12. (a) Line half-widths are plotted versus incident energy T_0 at the angles θ specified. These correspond to the half-width of the profile measured at $1/e$ times the peak height. Here δQ is the half-width of the measured C_{TT} profile, and δQ_a is the instrumental contribution. The thermal contribution δQ_t is also shown. (b) The solid points show the over-all natural half-width δQ^N plotted versus $\bar{Q}$. The crossed points indicated the natural half-width $\delta Q_{mn}{}^N$ of individual (m,n) reactions, but the accuracy of these is subject to large error. In both cases the indicated half-widths are those at $1/e$ height on the profile.

approach the same angular half-width. In our apparatus, the average of many measurements show this half-width to equal 0.40°, or 0.070 rad. Correspondingly, $\delta Q_a = (0.070)\, T_0 \sin 2\theta$, following Eq. (5). The dotted line in Fig. 12(a) shows δQ_a plotted versus T_0 for the angles θ specified.

Second, there is the effective half-width δQ_t due to the thermal motion of the target atoms. Appendix C shows that δQ_t is independent of θ but proportional to $T_0{}^{1/2}$, as given by Eq. (C9). The dashed line in Fig. 12(a) shows δQ_t versus T_0. Although the thermal broadening is largest, numerically, at high energies it has the largest proportionate effect at low energies and small scattering angles where it predominates over instrumental broadening.

Third, there is a "natural" half-width, δQ^N. Each data set contains many (m,n) reactions which center on different values $\bar{Q}_{mn}$ so that the over-all Q distribution must have a certain half-width.

If one assumes that each of these three broadening effects is an independent Gaussian curve, then

$$(\delta Q)^2 = (\delta Q_a)^2 + (\delta Q_t)^2 + (\delta Q^N)^2 . \tag{14}$$

In this equation δQ^N is the only quantity not shown in Fig. 12(a). Equation (14) can be used to compute δQ^N for each data set, and this is shown plotted versus $\bar{Q}$ in Fig. 12(b). On the left side of this plot δQ^N is fairly accurate. However, on the right side, where the instrumental broadening predominates, the estimated error in δQ^N becomes very large. The error bars correspond to a $\pm 0.036°$ error in measurement of angular half-width.

Each of the individual (m,n) contours, such as the C_{33} and C_{35} cases shown in Fig. 3(b) also have an experimental half-width. An attempt was made to study the corresponding natural half-widths $\delta Q_{mn}{}^N$ in the same manner as above, but this met limited success. At 3 keV, 8° and 6 keV, 8° the individual (m,n) reactions appeared to have natural half-widths in the range of 0 to 12 eV, considerably more narrow than the corresponding over-all natural half-widths δQ^N. At energies of 25 keV and above there was a large scatter to the measured half-widths even after taking averages within each data set. The corresponding values of natural half-widths $\delta Q_{mn}{}^N$ are shown as the points marked $\times$ on Fig. 12(b), but these points have little significance because the possible error assigned here (though not indicated on the figure) is practically larger than their value. The difficulty is that the individual C_{mn} contours represent many less counts than the C_{TT} contours and there is far less accuracy in the measured half-widths. From our data we cannot say with certainty whether the natural half-widths $\delta Q_{mn}{}^N$ for individual (m,n) reactions are very small or whether they are a reasonable fraction of the over-all natural half-width δQ^N.

ACKNOWLEDGMENTS

We thank Professor Arnold Russek for his continuing interest in these measurements. We are pleased to thank Miss Marianne Melnick, who helped take and reduce the data.

APPENDIX A: Q CALCULATION

The relationship between the inelastic energy and the two scattering angles will be derived in support of Eqs. (2)–(5) of Sec. 1. Account is taken of the momentum associated with the thermal motion of the target atom so that the equations here may be used also for the calculation of thermal lines widths in C below.

The equations conserving energy and momentum are

$$T_0 = T_1 + T_2 + Q , \tag{A1}$$

$$(\gamma T_0)^{1/2}(1+\epsilon_x) = (\gamma T_1)^{1/2}\cos\theta + T_1{}^{1/2}\cos(\beta-\theta) , \tag{A2}$$

and

$$(\gamma T_1)^{1/2}\sin\theta + \epsilon_y(\gamma T_0)^{1/2} = T_2{}^{1/2}\sin(\beta-\theta) . \tag{A3}$$

Here ϵ_x is the ratio of the initial x momentum of the target atom to the momentum of the incident particle, and ϵ_y refers to the y momentum of the target. These quantities are of the order of 10^{-3}. Eliminating T_2 between Eqs. (A2) and (A3), one obtains

$$(T_1/T_0)^{1/2} = [(1+\epsilon_x)\sin(\beta-\theta) - \epsilon_y\cos(\beta-\theta)]/\sin\beta , \tag{A4}$$

and, similarly,

$$(T_2/T_0)^{1/2}=\gamma^{1/2}[(1+\epsilon_x)\sin\theta+\epsilon_y\cos\theta]/\sin\beta. \quad \text{(A5)}$$

Equation (4) of the text is the same as Eq. (A1) here. Setting $\epsilon_x=\epsilon_y=0$ in Eqs. (A4) and (A5) leads to Eqs. (3) and (4), respectively.

The approximate expression, Eq. (5), is the $\gamma=1$ case of a more general expression, which is derived next. When Eqs. (2)–(4) are solved for Q the well-known result[1] is

$$Q(\beta)=T_0-T_0[\sin^2(\beta-\theta)+\gamma\sin^2\theta]/\sin^2\beta. \quad \text{(A6)}$$

Here, as in the experiment, θ is regarded as being fixed, and the value of Q depends on the angle β at which the second particle is observed. Let β_0 be the angle corresponding to $Q=0$, and this may be found from

$$\begin{aligned}\sin^2(\beta_0-\theta)+\gamma\sin^2\theta&=\sin^2\beta_0, \quad \gamma\neq 1\\ \beta_0&=\pi/2, \quad \gamma=1.\end{aligned} \quad \text{(A7)}$$

When $Q(\beta)$ of Eq. (A6) is expanded about β_0, the first term, $Q(\beta_0)$ is zero so that

$$Q(\beta)=(\beta_0-\beta)K(\beta_0)+\cdots, \quad \text{(A8)}$$

where

$$K(\beta_0)=[-dQ/d\beta]_{\beta=\beta_0}. \quad \text{(A9)}$$

Equation (A8) shows that in general the Q value, to first order, is proportional to the departure of β from β_0. In practice, when $\gamma\neq 1$, the computation of β_0 and $K(\beta_0)$ is sufficiently involved that it is easier to use Eq. (A6), which is exact. For the case $\gamma=1$, however, where β_0 is $\pi/2$, it may be shown that

$$K(\pi/2)=T_0\sin 2\theta. \quad \text{(A10)}$$

When this is substituted into Eq. (A8), the result is Eq. (5).

APPENDIX B: INDIVIDUAL PARTICLE ENERGIES

It is necessary to know T_1 and T_2 individually not only to allow for the time of flight but also in order to set the potentials of both charge-state analyzers. The kinetic energies of scattered particles vary approximately as the cosine-squared of the angle between the incident beam and the detector in question, but this is true only for noncoincidence events. That is, most of the particles seen in one detector are not in coincidence with particles seen in the other detector. The subset of particles corresponding to coincidence events at angles (θ,β) have a different energy dependence because of the various Q values within that subset. The applicable formulas are given by Eqs. (2) and (3).

For the $\gamma=1$ case, where β is near $\pi/2$ and $\sin^2\beta\approx 1$, it is seen from Eq. (3) that T_2 is dependent only on θ, and from Eq. (2) that T_1 depends on both θ and β. In the experiments θ is held constant and there is the surprising fact that as the angle β of the recoil detector is swept the recoil energy T_2 remains constant, whereas the energy T_1 of the scattered particle (whose angle θ is constant) varies somewhat with β.

The practical result of these considerations is that it is not correct to set the schedule of voltages of the charge state analyzers by maximizing the current of the successive charge states seen in noncoincidence. A rather different (and correct) schedule of voltages for the recoil box is obtained by maximizing the current of successive charge states as seen in coincidence with particles detected in the scattering box. This same schedule of voltages is then used without change as β is swept at fixed θ.

APPENDIX C: EFFECT OF THERMAL TARGET MOTION

Although the thermal energy of the target atom is negligible and does not appear in Eq. (A1), the momentum due to thermal motion causes "linewidth" effects which are not negligible. When Eqs. (A4) and (A5) are squared and terms in ϵ^2 are discarded, one obtains, upon substitution into Eq. (A1):

$$\begin{aligned}Q/T_0=1-[(1-2\epsilon_x)\sin^2(\beta-\theta)-\epsilon_y\sin 2(\beta-\theta)]/\sin^2\beta\\ -\gamma[(1-2\epsilon_x)\sin^2\theta+\epsilon_y\sin 2\theta]/\sin^2\beta.\end{aligned} \quad \text{(C1)}$$

This reduces to Eq. (A6) when $\epsilon_x=\epsilon_y=0$.

Equation (C1) does not include ϵ_z. Target momentum perpendicular to the original plane of collision causes the scattered and recoil particle to lie in a new plane which is not perpendicular to the axis of rotation of the instrument, and which, in general, does not contain the incident beam. The primary effect of this is a loss in coincidence counts, not a broadening of resolution, and so this will not be considered here in detail.

The consequences of target thermal motion can be isolated by considering both detectors to have substantially zero-angular resolution widths and by taking Q to be a constant. Holding θ fixed and sweeping β, one would obtain a coincidence-count peak such as the (T,T) curve shown in Fig. 3(b) except that it would be more narrow, the entire width being caused by thermal effects. Here $Q/T_0\ll 1$, and the resulting half-width δQ_t, defined as the half-width at $1/e$ of the peak height, can be shown to be substantially the same whether Q is finite or zero. That is, if Q were zero, the (T,T) curve in Fig. 3(b) would be centered on $\beta_0=90°$, but would be of the same width. In the general case, where $\gamma\neq 1$, the coincidence count curve would be centered on β_0 as given by Eq. (A7) when $Q=0$.

The quantity $\eta=\beta_0-\beta$ is small and Eq. (C1) may be expanded about β_0, discarding terms in ϵ^2, $\epsilon\eta$, and η^2. The result (for $Q=0$) is

$$\eta=\beta_0-\beta=T_0[2\epsilon_x-\epsilon_y f(\beta_0)]/K(\beta_0), \quad \text{(C2)}$$

where

$$f(\beta_0)=[\sin(2\beta_0-2\theta)-\gamma\sin 2\theta]/\sin^2\beta_0, \quad \text{(C3)}$$

and where $K(\beta_0)$ is given by Eq. (A9). When $\gamma \neq 1$, both β_0 and the slope $K(\beta_0)$ are most easily obtained numerically from a plot of Eq. (A6). In the present Ar^+-Ar case, where $\gamma=1$ and $\beta_0=\pi/2$, one finds $f(\pi/2)=0$ and $K(\pi/2)=T_0 \sin 2\theta$. Thus, Eq. (C2) reduces to

$$\beta_0-\beta=2\epsilon_x/\sin 2\theta, \tag{C4}$$

for $\gamma=1$.

The next step is to relate ϵ_x to the temperature t. The number of target particles dN having x momentum in the range $d\epsilon_x$ is given by

$$dN/d\epsilon_x=(\text{const})\exp[-\epsilon_x^2 T_0/kt], \tag{C5}$$

where k is Boltzmann's constant. Equation (C4) shows that $\beta_0-\beta$ is proportional to ϵ_x so that the line shape will be Gaussian as in Eq. (C5). The $1/e$ height in Eq. (C5) occurs at a particular value ϵ_x' where the exponent has unit magnitude. Thus

$$\epsilon_x'=(kt/T_0)^{1/2}. \tag{C6}$$

Using Eq. (C4) one finds that the corresponding half-width $\delta\beta_t$ is given by

$$\delta\beta_t=2\epsilon_x'/\sin 2\theta=2(kt)^{1/2}/(T_0^{1/2}\sin 2\theta). \tag{C7}$$

The relationship between Q and β is linear in the region of β_0, and there is a half-width δQ_t of the distribution in Q corresponding to $\delta\beta_t$. Thus, using Eq. (5),

$$\delta Q_t=\delta\beta_t T_0 \sin 2\theta. \tag{C8}$$

When this is combined with Eq. (C7) there is an extremely simple result:

$$\begin{aligned}\delta Q_t&=2(T_0 kt)^{1/2}\\&=(0.010)T_0^{1/2}.\end{aligned} \tag{C9}$$

The numerical factor, 0.010, is to be used when both δQ_t and T_0 are in keV and when t is room temperature, or 300°K. A thermal half-width (at $1/e$ height) δQ_t of 0.072 keV is predicted at $T_0=50$ keV and 0.023 keV at $T_0=5$ keV. Neither of these widths is negligible at the energies in question. There would be some advantage if the gas target region were at low temperature, since these half-widths, as seen in Eq. (C9), scale as the square root of the temperature.

PHYSICAL REVIEW VOLUME 146, NUMBER 1 3 JUNE 1966

Statistical Model for the Ar^+-on-Ar Collision*

EDGAR EVERHART AND QUENTIN C. KESSEL
Physics Department, The University of Connecticut, Storrs, Connecticut
(Received 23 November 1965; revised manuscript received 1 March 1966)

This paper introduces a model to describe and predict the preceding experimental results on Ar^+—Ar scattering. In considering a number of collisions in a data set it is assumed that there is a distribution among the inelastic energies of the atoms after the collision. It is further assumed that the energy received by one atom is not correlated with the energy received by the other atom in the same collision. The model, whose distribution widths are fitted to the data, predicts the average inelastic energy loss $\bar{Q}_{mn}$ associated with a collision which results in one atom becoming m times ionized and the other n times ionized. The relative abundance $\bar{p}_{mn}$ of the (m,n) reaction is also predicted. The values of $\bar{Q}_{mn}$ and $\bar{p}_{mn}$ so predicted agree well with the data. The model allows derivation from the data of the probability P_i that an atom, which received a particular inelastic energy E, subsequently becomes i times ionized. These derived $P_i(E)$ curves are rather similar in form to those which have been calculated by Russek. Under some circumstances there is a triply peaked structure to the inelastic energies transferred in these collisions. This structure is explained within the framework of the present model. Indirect evidence is presented that in the more violent collisions there may be one fast electron emitted per atom whose kinetic energy is a sizeable fraction of the inelastic energy.

1. INTRODUCTION

THE coincidence measurements of Ar^+—Ar collisions of the preceding paper[1] are presented in a way so as to be independent of the model used to describe the collision. In the present paper we analyze and correlate these data. The model presented here is a further development along the lines of our recent letters.[2,3]

Starting with the concepts of the Russek[4] theory of statistical distribution of energy to the several electrons on an atom, our model includes also the effect of sta-

* This study was supported by the U. S. Air Force Office of Scientific Research.

[1] Q. C. Kessel and E. Everhart, preceding paper, Phys. Rev. **146**, 16 (1966).

[2] E. Everhart and Q. C. Kessel, Phys. Rev. Letters **14**, 247 (1965).

[3] Q. C. Kessel, A. Russek, and E. Everhart, Phys. Rev. Letters **14**, 484 (1965).

[4] A. Russek and M. T. Thomas, Phys. Rev. **109**, 2015 (1958); **114**, 1538 (1959); J. B. Bulman and A. Russek, *ibid.* **122**, 506 (1961); A. Russek, *ibid.* **132**, 246 (1963).